Opto-Electronic Advances

CN 51–1781/TN ISSN 2096–4579 (Print) ISSN 2097–3993 (Online)

Spatiotemporal multiplexed photonic reservoir computing: parallel prediction for the high-dimensional dynamics of complex semiconductor laser network

Tong Yang, Li-Yue Zhang, Song-Sui Li, Wei Pan, Xi-Hua Zou and Lian-Shan Yan

Citation: Yang T, Zhang LY, Li SS, et al. Spatiotemporal multiplexed photonic reservoir computing: parallel prediction for the high-dimensional dynamics of complex semiconductor laser network. *Opto-Electron Adv* **8**, 250159(2025).

https://doi.org/10.29026/oea.2025.250159

Received: 23 June 2025; Accepted: 29 September 2025; Published online: 14 November 2025

Opto-Electronic Advances

Article

December 2025, Vol. 8, No. 12

DOI: 10.29026/oea.2025.250159 CSTR: 32247.14.oea.2025.250159

Spatiotemporal multiplexed photonic reservoir computing: parallel prediction for the high-dimensional dynamics of complex semiconductor laser network

Tong Yang, Li-Yue Zhang*, Song-Sui Li, Wei Pan, Xi-Hua Zou and Lian-Shan Yan*

Accurately forecasting the high-dimensional chaotic dynamics of semiconductor laser (SL) networks is essential in photonics research. In this study, we propose a spatiotemporal multiplexed photonic reservoir computing (STM-PRC) architecture, specifically designed for parallel prediction of the high-dimensional chaotic dynamics in complex SL networks. This is accomplished by decomposing the prediction task into multiple simplified reservoirs, leveraging the intrinsic topological characteristics of the network. Additionally, we introduce a dimensionality reduction technique for high-dimensional chaotic datasets, which exploits the symmetrical properties of the network topology and cluster synchronization patterns derived from complex network theory. This approach further simplifies the prediction process and enhances the computational efficiency of the parallel STM-PRC system. The feasibility and effectiveness of the proposed framework are demonstrated through numerical simulations and corroborated by experimental validation. Our results expand the application potential of SL networks in all-optical communication systems and suggest new directions for optical information processing.

Keywords: photonic reservoir computing; complex network; semiconductor lasers

Yang T, Zhang LY, Li SS et al. Spatiotemporal multiplexed photonic reservoir computing: parallel prediction for the high-dimensional dynamics of complex semiconductor laser network. *Opto-Electron Adv* **8**, 250159 (2025).

Introduction

Chaotic dynamics generated by semiconductor lasers (SLs) have attracted significant attention due to their diverse applications. These nonlinear phenomena have been extensively studied in areas such as chaotic secure communication, high-speed physical random number generation, and photonic neuromorphic computing[1–13]. Over the past decades, various methods have been developed to predict the chaotic dynamics of SLs. Traditional model-based approaches typically involve constructing simplified nonlinear mathematical models derived from known physical principles or reconstructing the underlying dynamics from empirical observations[14–16]. However, these approaches often rely on empirical assumptions about chaotic systems. Owing to incomplete representations of key dynamics and limitations in system dimensionality, their application can lead to substantial prediction errors[17].

Center for Information Photonics and Communications, Southwest Jiaotong University, Chengdu 610031, China.
*Correspondence: LY Zhang, E-mail: lyzhang@swjtu.edu.cn; LS Yan, E-mail: lsyan@home.swjtu.edu.cn
Received: 23 June 2025; Accepted: 29 September 2025; Published online: 14 November 2025

To address these limitations, machine learning has emerged as a powerful data-driven alternative for forecasting chaotic behavior. By learning directly from observational data and leveraging strong nonlinear computational capabilities, machine learning methods can achieve accurate predictions in complex systems[18–21]. Among these approaches, reservoir computing (RC) is particularly notable for its simplicity, computational efficiency, and effectiveness in modeling and predicting chaotic dynamics[22–25]. RC has also been utilized as a state observer to perform cross-prediction of unmeasured variables in chaotic SL systems[26]. As a specialized form of recurrent neural network, RC typically consists of three layers: an input layer, a reservoir layer, and an output layer. The input weights and internal connections of the reservoir are randomly generated and fixed, while only the output weights require training through a simple algorithm. This design not only accelerates computation but also significantly reduces resource requirements. As a result, RC has been widely applied in forecasting chaotic spatiotemporal sequences, such as those generated by SLs. Photonic reservoir computing (PRC), inspired by neurocomputational mechanisms, extends the RC framework by exploiting the nonlinear properties and high-dimensional state spaces of optical systems to perform efficient computations[27–32]. A notable implementation of PRC is time-delay reservoir computing (TDRC), which employs a nonlinear node to map spatial interactions into temporal sequences, thereby simplifying the hardware design. Extensive research has demonstrated that TDRC systems, utilizing semiconductor lasers as nonlinear physical nodes, can achieve high accuracy in chaotic time-series prediction tasks[33–38]. Recent advances have demonstrated the potential of RC in predicting the chaotic dynamics of SLs. Numerical studies have successfully predicted the amplitudes of upcoming emitted chaotic pulses[39], as well as the continuous intensity time series and the underlying dynamical behavior of chaotic SLs[40]. Furthermore, recent studies have proposed a single-node PRC approach that forecasts the chaotic behavior of external cavity SLs based solely on observed data[41]. Experimental validation has also demonstrated the effectiveness of TDRC in predicting chaotic time series generated by SLs[42,43]. On the other hand, traditional TDRC has demonstrated strong performance in predicting chaotic signals. However, most studies have concentrated on low-dimensional time series. When directly applied to forecasting the high-dimensional dynamics of large complex networks, TDRC often encounters substantial limitations, including reduced prediction accuracy, the requirement for an excessive number of virtual nodes, and slow information processing. Moreover, regarding chaotic signals generated by SLs, existing research has primarily focused on predicting the chaotic dynamics of isolated SLs, while the prediction of high-dimensional chaotic signals in SL networks has not yet been thoroughly investigated. Therefore, applying RC to achieve lightweight, high-speed, and accurate prediction of large-scale complex chaotic systems， such as SL networks，remains an important direction for further exploration.

In this work, we propose and experimentally validate a parallel PRC architecture based on spatiotemporal multiplexing for accurate forecasting of the high-dimensional chaotic dynamics in complex SL networks. By exploiting the intrinsic topological features of the network, the high-dimensional prediction task is decomposed into multiple simplified reservoirs operating in parallel, enabling enhanced predictive accuracy and computational efficiency across various network scales. To further facilitate hardware implementation, a dimensionality reduction strategy tailored for high-dimensional chaotic datasets is introduced based on the inherent symmetry of network topology. Finally, the feasibility and effectiveness of the proposed framework are confirmed through comprehensive experimental validation.

Methodology

Generation of chaotic dynamics in complex SL network

In this paper, the SL network under consideration is modeled as a homogeneous and undirected network. Using graph-theoretic methods from the field of complex networks, the coupling interactions between SLs are mathematically represented by an adjacency matrix $\boldsymbol{A}$. Specifically, if there exists a mutual coupling link between lasers SL_m and SL_l, the corresponding elements of the matrix are defined as $\boldsymbol{A}_{m,l} = \boldsymbol{A}_{l,m} = 1$. Conversely, if no coupling exists between lasers m and l, the elements are set to $\boldsymbol{A}_{m,l} = \boldsymbol{A}_{l,m} = 0$[44]. The dynamics of each node in the network are governed by the Lang-Kobayashi equations[45]. By incorporating the adjacency matrix into the model, the rate equations for the SL network are formulated as follows:

$$\begin{aligned} E_m(t) =& \frac{(1+\mathrm{i}\alpha_m)}{2}\left(G_m-\frac{1}{\tau_{\mathrm{p},m}}\right)E_m(t) \\ &+ k_{\mathrm{f},m}E_m(t-\tau_{\mathrm{f},m})\exp(-\mathrm{i}\omega_m\tau_{\mathrm{f},m}) \\ &+ \sigma_m\sum_{j}^{D_\mathrm{s}}A_{ml}E_l(t-\tau_m)\exp(-\mathrm{i}\omega_l\tau-\mathrm{i}2\pi\Delta f t) \\ &+ \sqrt{2\beta_m N_m(t)}\chi_m(t)\ , \end{aligned} \tag{1}$$

$$\begin{aligned} N_m(t) =& p_{\mathrm{f},m}J_\mathrm{th}-\frac{N_m(t)}{\tau_\mathrm{e}}-G_m\|E_m(t)\|^2 \\ & m,l=1,\ldots,D_\mathrm{s}\ , \end{aligned} \tag{2}$$

where E_m and N_m are the complex electronic field and the carrier number of SL_m, respectively. α_m is the linewidth enhancement factor, $G_m(t)=g[N_m(t)-N_0]/(1+s\|E_m(t)\|^2)$ is the optical gain, $g=1.5\times10^{-8}\ \mathrm{ps}^{-1}$ is differential gain, $N_0=1.5\times10^8$ is transparency carrier density, $s=5\times10^{-7}$ is nonlinear saturation coefficient, $\tau_{\mathrm{p},m}=2$ ps is photon lifetime, $\tau_m=1$ ns is the coupling delay between SLs, $\tau_{\mathrm{f},m}=1$ ns is self-feedback delay, $k_{\mathrm{f},m}$ is the self-feedback strength, ω_m is the reference frequency corresponding to $\lambda=1550$ nm, σ_m stands for the uniform coupling strength, β_m is spontaneous emission rate, $\chi_m(t)$ is the Gaussian noise with unity variance and zero mean, We note that the results in this work are evaluated without noise, however the term of noise is presented to elucidate that the scheme is robust. D_s represents the number of SLs in the network, $p_{\mathrm{f},m}$ is the current factor, $\tau_\mathrm{e}=2$ ns is carrier lifetime[44]. To evaluate the prediction performance of the proposed STM-PRC architecture in comparison with the conventional TDRC, we consider a network composed of 8 SLs as a representative example. The network topology, as defined by the adjacency matrix $\boldsymbol{A}$ is shown in Fig. 1(a) and Fig. 1(b), respectively, while Fig. 1(c) presents the corresponding temporal waveforms of each SL under the conditions of current factor $p_{\mathrm{f},m}$=2.5, an optical feedback strength $k_{\mathrm{f},m}$= 5 ns^{-1}, and uniform coupling strength σ_m= 15 ns^{-1}.

Spatial-temporal multiplexing photonic reservoir computing

We first present the schematic of a conventional TDRC system used for predicting high-dimensional time series. As illustrated in Fig. 2, a standard TDRC architecture consists of three key components: an input layer, a reservoir layer, and an output layer. In the input layer, the input signal $u(t)\in\mathbb{R}^d$ is multiplied by an input weight matrix $\boldsymbol{W}_\mathrm{in}\in\mathbb{R}^{d\times N}$ to generate the input matrix $\boldsymbol{S}(t)$.

$$\begin{aligned} \boldsymbol{S}(t) =& \boldsymbol{u}(t)\times\boldsymbol{W}_\mathrm{in}\ , \\ \boldsymbol{W}_\mathrm{in} =& \boldsymbol{\gamma}\times\boldsymbol{mask}(t)\ , \end{aligned} \tag{3}$$

where, the mask(t) is a binary random matrix of dimensions $d\times N$ with elements drawn from $\{0.1, 1\}$[43,46], where d denotes the dimensionality of the input time series with d = 8, and N denotes the number of virtual nodes in TDRC system. Linear scaling of the input matrix is achieved by adjusting the parameter $\boldsymbol{\gamma}$.

In the reservoir layer, the drive laser is modulated by input matrix $\boldsymbol{S}(t)$ through an intensity modulator and subsequently injected into the reservoir laser within a time-delay loop. This delay loop contains N virtual nodes, spaced by a time interval $\theta=\tau_\mathrm{r}/N$, where τ_r represents the self-feedback delay time of reservoir laser. Consequently, each node state $X_i(t),(i=1,2,\ldots,N)$ corresponds to the transient response of reservoir laser. Over the entire feedback delay time τ_r, these node states collectively form a high-dimensional vector. Thus, the input data $\boldsymbol{S}(t)$ are nonlinearly mapped into an N-dimensional space. Previous studies have shown that TDRCs do not require a predefined relationship between the clock cycle and the delay time. This

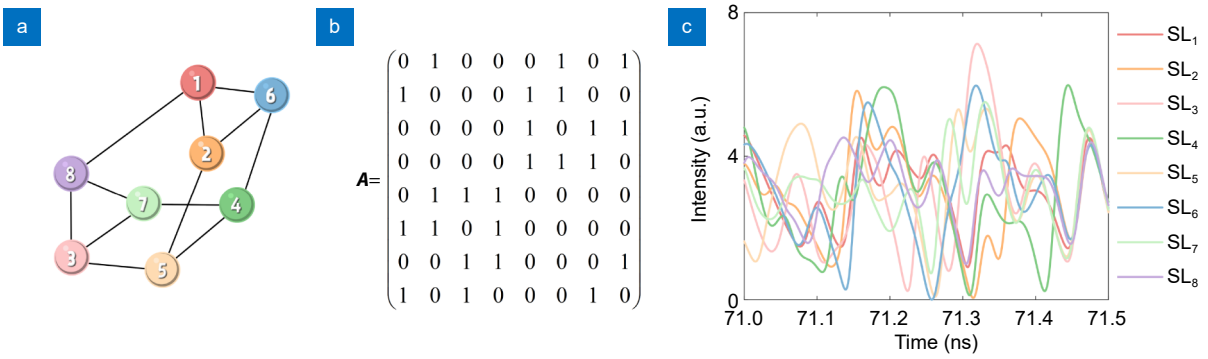

Fig. 1 | (**a**) Topology of the network for prediction. (**b**) Adjacency matrix of the SL network. (**c**) Dynamical evolution of SLs within the network in a specific time interval, as shown in (a).

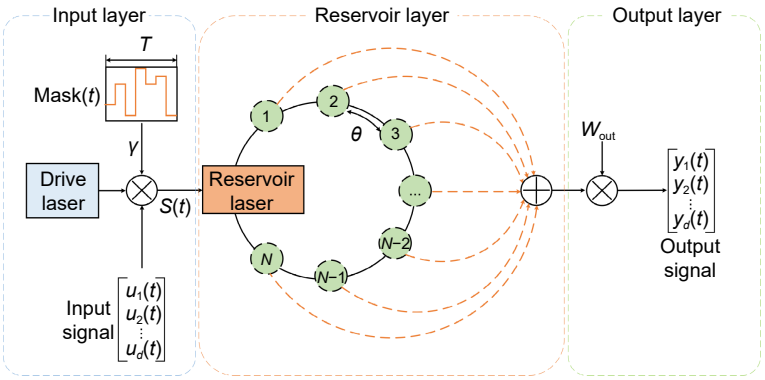

Fig. 2 | The operation procedure of conventional TDRC.

independence between the two timescales provides greater flexibility for hardware implementation[47]. In this work, we adopt the classical asynchronous configuration $\tau_r = T + \theta$. The dynamics of the optically injected reservoir laser can be described by the Lang-Kobayashi equations as follows[45]:

$$\begin{aligned}\frac{\mathrm{d}E_\mathrm{r}(t)}{\mathrm{d}t} =& \frac{1}{2}(1+\mathrm{i}\alpha_\mathrm{r})\left\{\frac{G_N(N_\mathrm{r}(t)-N_0)}{1+\varepsilon_\mathrm{r}|E_\mathrm{r}(t)|^2}-\frac{1}{\tau_{p,\mathrm{r}}}\right\}E_\mathrm{r}(t)\\&+k_{\mathrm{f,r}}E_\mathrm{r}(t-\tau_\mathrm{r})\exp(-\mathrm{i}2\pi f_0\tau_\mathrm{r})\\&+k_{\mathrm{in,r}}E_\mathrm{s}(t)\exp(\mathrm{i}2\pi\Delta f_\mathrm{s}t)+\sqrt{2\beta_\mathrm{r}N_\mathrm{r}(t)}\chi_\mathrm{r}(t)\ ,\end{aligned} \tag{4}$$

$$\frac{\mathrm{d}N_\mathrm{r}(t)}{\mathrm{d}t} = p_{\mathrm{f,r}}J_\mathrm{th}-\frac{N_\mathrm{r}(t)}{\tau_\mathrm{s}}-\frac{G_N(N_\mathrm{r}(t)-N_0)}{1+\varepsilon_r|E_r(t)|^2}|E_\mathrm{r}(t)|^2\ , \tag{5}$$

where $E_\mathrm{r}(t)$ and $N_\mathrm{r}(t)$ denote the complex electric field amplitude and the carrier density of the reservoir laser, respectively. $E_\mathrm{s}(t)=\sqrt{I_d}\left(1+\mathrm{e}^{\mathrm{i}S(t)}\right)/2$ is the output of drive laser which is modulated by $S(t)$, and we employ intensity modulation to inject the input data into the reservoir. β_r is spontaneous emission rate, $\chi_\mathrm{r}(t)$ is the Gaussian noise with unity variance and zero mean, we note that the results in this work are evaluated without noise, however the term of noise is presented to elucidate that the scheme is robust. $k_{\mathrm{f,r}}$ indicates the self-feedback strength of reservoir laser and $k_{\mathrm{in,r}}$ describes the injection strength from driver laser. $p_{\mathrm{f},r}$ denotes the current factor of reservoir laser and Δf_s is the frequency detuning between drive laser and reservoir laser. The other typical parameters of the reservoir laser are summarized in Table 1[48].

In the output layer, the output vector $y(t+\Delta t)\in\mathbb{R}^d$ is computed as a linear combination of the state vector $X(t)$ of the virtual nodes and the output connection weight matrix $\boldsymbol{W}_\mathrm{out}(t)\in\mathbb{R}^{d\times N}$, expressed as:

$$y(t+\Delta t) = \boldsymbol{W}_\mathrm{out}\times\boldsymbol{X}(t)\ . \tag{6}$$

To determine the output connection weight matrix $\boldsymbol{W}_\mathrm{out}(t)$, we employ the ridge regression algorithm as follows:

$$\boldsymbol{W}_\mathrm{out} = \left(\boldsymbol{X}^\mathrm{T}\boldsymbol{X}+\lambda\boldsymbol{I}\right)^{-1}\boldsymbol{X}^\mathrm{T}u(t)\ , \tag{7}$$

where $\boldsymbol{I}$ denotes the N-dimensional identity matrix and λ is the ridge regression parameter. Typically, the optimal value of λ is selected via cross-validation based on test samples to avoid overfitting, and is set to 5×10^{-6} in this study.

Although conventional TDRC has demonstrated

Table 1 | Parameter values used for numerical calculation in TDRC and STM-PRC.

Parameter	Symbol	Value
Photon lifetime	$\tau_{p,r}$	1.927 ps
Carrier lifetime	τ_s	2.04 ns
Gain saturation	ε_r	2.0×10^{-23}
Gain coefficient	G_N	8.4×10^{-13} m^3·s^{-1}
Linewidth enhancement factor	α_r	3
Intensity of light source	Id	6.56×10^{20}
Threshold current of the response lasers	J_{th}	0.9892×10^{33} m^{-3}·s^{-1}
Carrier density at transparency	N_0	1.4×10^{24} m^{-3}
Node internal	θ	10 ps

relatively good performance in predicting the chaotic dynamics of SLs, its effectiveness is constrained as the dimensionality of the input signal increases. While increasing the number of virtual nodes can moderately improve prediction accuracy, it also significantly hinders processing speed, limiting the system's scalability and real-time applicability.

Therefore, we propose a highly efficient spatiotemporal multiplexed photonic reservoir computing (STM-PRC) framework based on conventional TDRC, as depicted in Fig. 3. In this framework, each SL_i in the target network is equipped with its own dedicated reservoir R_i parallelly. In the input layer, the input signal $\boldsymbol{u}_{p,i}(t)$ to each reservoir includes the temporal signal from its associated SL_i as well as additional signals from directly coupled neighboring SLs of SL_i. In this way, the spatial information of the network topology is multiplexed. Specifically, the temporal dynamics of a given node serve as the primary input to the reservoir associated with that node itself. On the other hand, they are also spatially multiplexed as supplementary input signals to the reservoirs of its directly coupled neighbors. The number of such neighbors is equal to the node's degree D_i. Therefore, the input dimensionality is elevated from the traditional TDRC's input $\boldsymbol{u}(t) \in \mathbb{R}^d$ to $\boldsymbol{u}_{p,i}(t) \in \mathbb{R}^{D_i+1}$ now. Accordingly, the input weight matrix is changed to $\boldsymbol{W}_{\text{in},i} \in \mathbb{R}^{(D_i+1)\times N_i}$:

$$\begin{aligned} \boldsymbol{u}_{\text{p},i}(t) &= \begin{bmatrix} u_i(t) \\ \sum u_{\text{coupled},i}(t) \end{bmatrix} , \\ \boldsymbol{S}_i(t) &= \boldsymbol{u}_{\text{p},i}(t) \times \boldsymbol{W}_{\text{in},i} , \\ \boldsymbol{W}_{\text{in},i} &= \boldsymbol{\gamma} \times \text{mask}_i(t) , \end{aligned} \tag{8}$$

where, taking the prediction of chaotic dynamics in SL_6 as an illustrative example, the inputs to reservoir R_6 are the signal of SL_6 itself, as well as that of directly connected neighbors: SL_1, SL_2, and SL_4. Hence, reservoir R_6 processes a four-dimensional input dataset defined as $\boldsymbol{u}_{\text{p},6}(t) = [u_6(t),\ u_1(t),\ u_2(t),\ u_4(t)]^{\text{T}}$. The implementation of reservoir layer in STM-PRC scheme is consistent with the conventional TDRC model as described previously. In the output layer, in contrast to conventional TDRC methods employing a "multi-input, multi-output" configuration, the proposed parallel STM-PRC architecture adopts a "multi-input, single-output" scheme, where

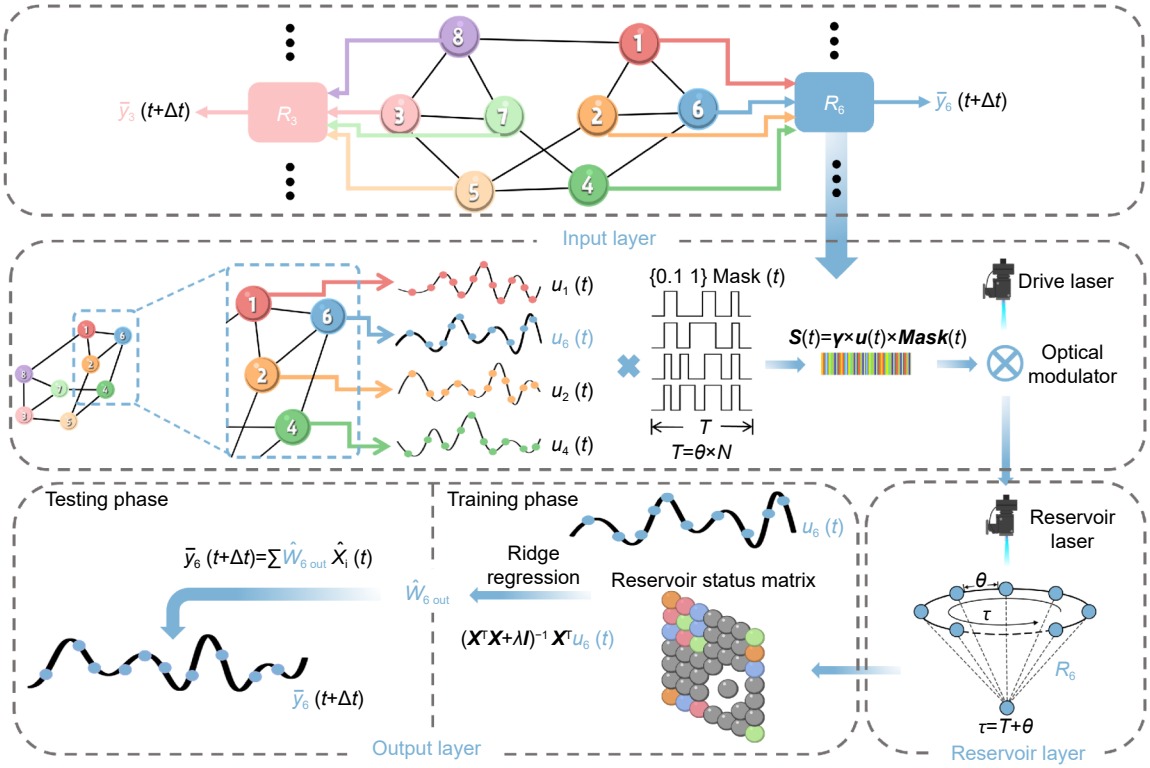

Fig. 3 | Schematic illustration of the STM-PRC architecture. Each node in the SL network is assigned an independent reservoir R_i. Reservoir (R_6) of SL_6 is highlighted as an example. Its input signal is derived by the corresponding node (SL_6) as well as its directly coupled neighbors (SL_1, SL_2, and SL_4). This process is the same for each SL in the predicted network. Each reservoir is independently trained to predict the temporal dynamics of its associated SL.

each R_i is individually trained to predict the specific dynamics of SL_i:

$$\begin{aligned} \boldsymbol{W}_{\text{out},i} &= \left(\boldsymbol{X}_i^{\mathrm{T}}\boldsymbol{X}_i + \lambda \boldsymbol{I}\right)^{-1}\boldsymbol{X}_i^{\mathrm{T}}\boldsymbol{u}_i(t) \ , \\ \boldsymbol{y}_{\text{p},i}\left(t+\Delta t\right) &= \boldsymbol{W}_{\text{out},i} \times \boldsymbol{X}_i\left(t\right) \ . \end{aligned} \tag{9}$$

As a result, the "true data" in the output layer consist exclusively of the one-dimensional time series from the target SL (in the case of SL_6, the "true data" correspond to $u_6(t)$). The output weight matrix $\boldsymbol{W}_{\text{out},i} \in \mathbb{R}^{1\times N_i}$ is still determined using ridge regression. And $\boldsymbol{y}_{\text{p},i}\left(t+\Delta t\right)$ represents the predicted dynamics of SL_i in STM-PRC. Thus, in parallel STM-PRC mechanism, each reservoir R_i is dedicated to predicting the dynamics of individual SL, which significantly reduces the number of virtual nodes required for accurate prediction. This in turn facilitates a simplified hardware implementation with improved processing speed. Moreover, the independence among parallel reservoirs allows for efficient parallelization, enhancing scalability and computational efficiency when applied to large-scale and complex SL networks. In addition, our extended analysis shows that introducing indirectly coupled SLs with reduced weights can further improve prediction performance under certain settings. Nevertheless, considering both prediction accuracy and the need to maintain a simple and lightweight architecture, in STM-PRC the input signal is ultimately derived from the node itself and its directly coupled neighbors.

The proposed STM-PRC scheme and the conventional TDRC scheme are evaluated under equivalent computational resource constraints, both utilizing an equal total number of virtual nodes $N = N_{\text{p},i} \times d$, while each configuration employs its respective optimal operational parameters. The evaluation is based on their ability to perform one-step-ahead prediction of the chaotic sequences in the SL network. To compare the effectiveness of different prediction schemes, the normalized mean-square error (NMSE) was employed as a metric for quantitatively quantifying the prediction accuracy:

$$NMSE = \frac{1}{L}\frac{\sum_{j=1}^{L}\left[y_i\left(j\right)-\bar{y}_i\left(j\right)\right]^2}{\sigma\left(\bar{y}_i\right)} \ , \tag{10}$$

where j represents the index of each data point in the time series, L denotes the length of test set time series, $y_i(j)$ refers to the data predicted by the STM-PRC system for SL_i, $\bar{y}_i(j)$ indicates the target values, and $\sigma(\bar{y}_i)$ represents the variance. The NMSE is obtained by calculating the average of the NMSE values across all nodes in the SL network to be predicted, with a lower NMSE value indicating superior predictive performance. The dynamics of the laser network in the dataset were generated under randomly chosen initial conditions, and the dataset used in our machine learning task is provided in supplementary information. Importantly, the prediction performance of the proposed reservoir remains independent of the specific initial conditions.

Results

Figure 4(a, b) compare the prediction performance of conventional TDRC and parallel STM-PRC architectures for the network shown in Fig. 1(a), using SL_6 as an illustrative example. The results clearly demonstrate that the conventional TDRC yields less accurate predictions (orange curve in Fig. 4(a)), whereas the STM-PRC produces highly accurate predicted signals (orange curve in Fig. 4(b)). Specifically, the STM-PRC architecture achieves a substantially lower NMSE of 0.0019, compared with 0.0744 for the conventional TDRC. Furthermore, we elucidate that this performance advantage remains consistent across the predictions of all other SLs in network. As shown in Fig. 4(c, d), the STM-PRC architecture maintains excellent prediction performance across all SLs in the network, underscoring its superior capability in reconstructing chaotic dynamics.

To quantitatively evaluate the advantages of this parallel scheme, Fig. 5 investigates the relationship between the prediction performance, information processing speed and training dataset size. And to mitigate fluctuations caused by random mask signals, average NMSE values are obtained from multiple mask realizations. Firstly, as the number of virtual nodes directly influences the reservoir's ability to adequately learn the features present in the training data, Fig. 5(a) plots the NMSE as a function of the number of virtual nodes at a fixed virtual node interval. Specifically, the red numerical values represent the number of virtual nodes per reservoir $N_{\text{p},i}$ in the STM-PRC, which is ranging from 20 to 200. While the blue values correspond to the equivalent total number of virtual nodes N in the conventional TDRC, ranging from 160 to 1600 with $N = N_{\text{p},i} \times d$. Specifically, the information processing rate is defined as $1/T$. For the STM-PRC architecture, each reservoir's processing time is calculated as $T = N_{\text{p},i} \times \theta$. In contrast, for traditional TDRC, the processing time is $T = (N_{\text{p},i} \times d) \times \theta$.

The corresponding information processing rates for

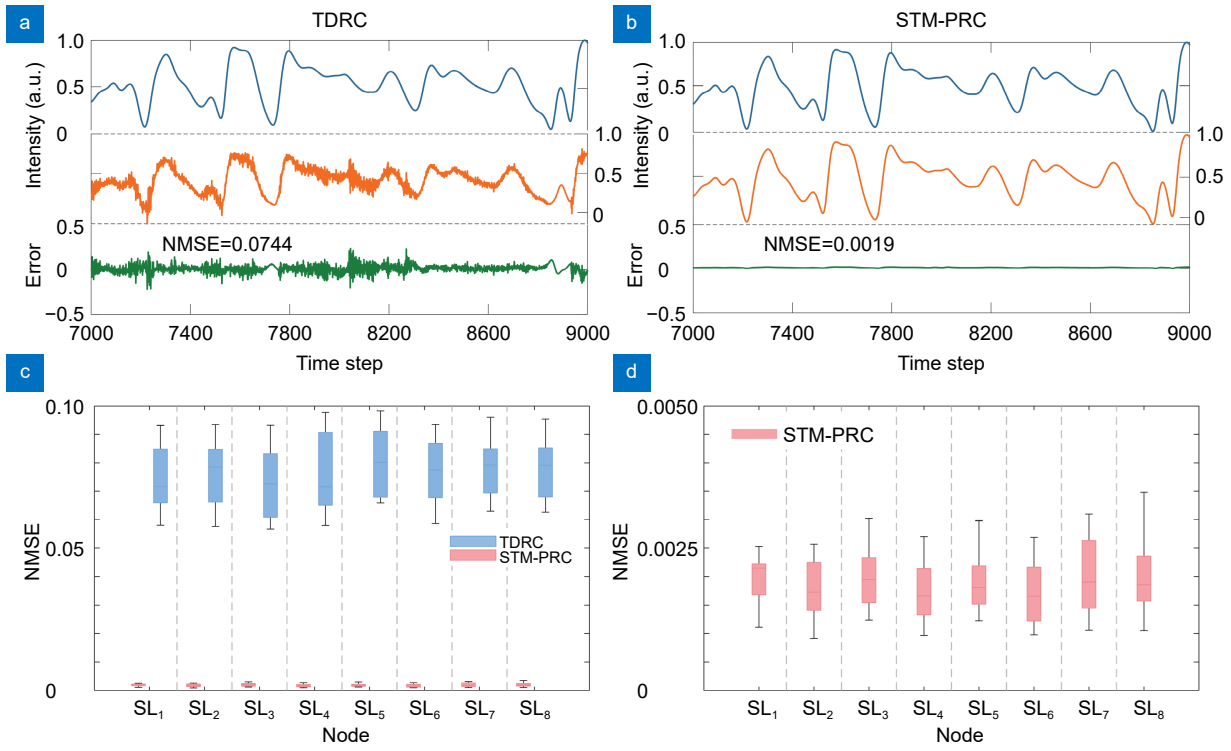

Fig. 4 | Comparison of prediction performance for the chaotic time series of complex SL networks under two reservoir computing configurations. The blue curve represents the ground truth, the orange curve depicts the predicted output signal, and the green curve illustrates the prediction error (i.e., the difference between actual and predicted values). (**a**) Results obtained using a conventional TDRC architecture with 800 virtual nodes, exemplified by SL_6. (**b**) Results obtained using a parallel STM-PRC architecture, each with 100 virtual nodes, exemplified by SL_6. (**c**) Comparison of prediction performance across network nodes between the conventional TDRC architecture and the parallel STM-PRC architecture consisting of eight independent reservoirs. (**d**) A zoomed-in view highlighting the enhanced performance achieved with the parallel STM-PRC architecture.

STM-PRC and TDRC are illustrated in Fig. 5(b), spanning 0.5–5 GSa/s and 0.0625–0.625 GSa/s, respectively. Since each reservoir R_i in the STM-PRC architecture is dedicated to predicting a single node, the required virtual node count $N_{p,i}$ per reservoir can be relatively small. As clearly indicated, compared to traditional TDRC, the STM-PRC architecture achieves higher prediction accuracy while significantly reducing the required number of virtual nodes. This reduction directly contributes to an approximately eightfold increase in information processing speed. Consequently, parallel STM-PRC mechanism could achieve an enhanced prediction performance with an equivalent computational investment compared to conventional TDRC. Moreover, the size of the training dataset plays a critical role in balancing prediction accuracy and training efficiency. As shown in Fig. 5(c), the STM-PRC consistently achieves notably lower NMSE values compared to conventional TDRC, thereby effectively improving training efficiency. Additionally, it can be found that the NMSE values tend to plateau when the training length surpasses about 12000 samples, this saturation phenomenon indicates that once the intrinsic memory capacity of the RC is exceeded, additional training data no longer contributes to improved prediction performance, and may even result in overfitting and performance stagnation.

To comprehensively demonstrate the significant advantages of the proposed STM-PRC architecture, we systematically compared its predictive performance against conventional TDRC across the operational parameter spaces of reservoir lasers ($p_f \times k_{f,r}$ and $\Delta f_s \times k_{in,r}$). Specifically, each reservoir within the STM-PRC was configured with the number of virtual nodes $N_{p,i} = 100$, while the conventional TDRC utilized a total of $N = 800$ virtual nodes. Figure 6(a) and 6(b) depict the variations of the NMSE for TDRC and STM-PRC architectures within the parameter space defined by current factor p_f and feedback strength $k_{f,r}$. Figure 6(c) and 6(d) further depict the dependence of NMSE on detuning frequency Δf_s and injection strength $k_{in,r}$ under a fixed current

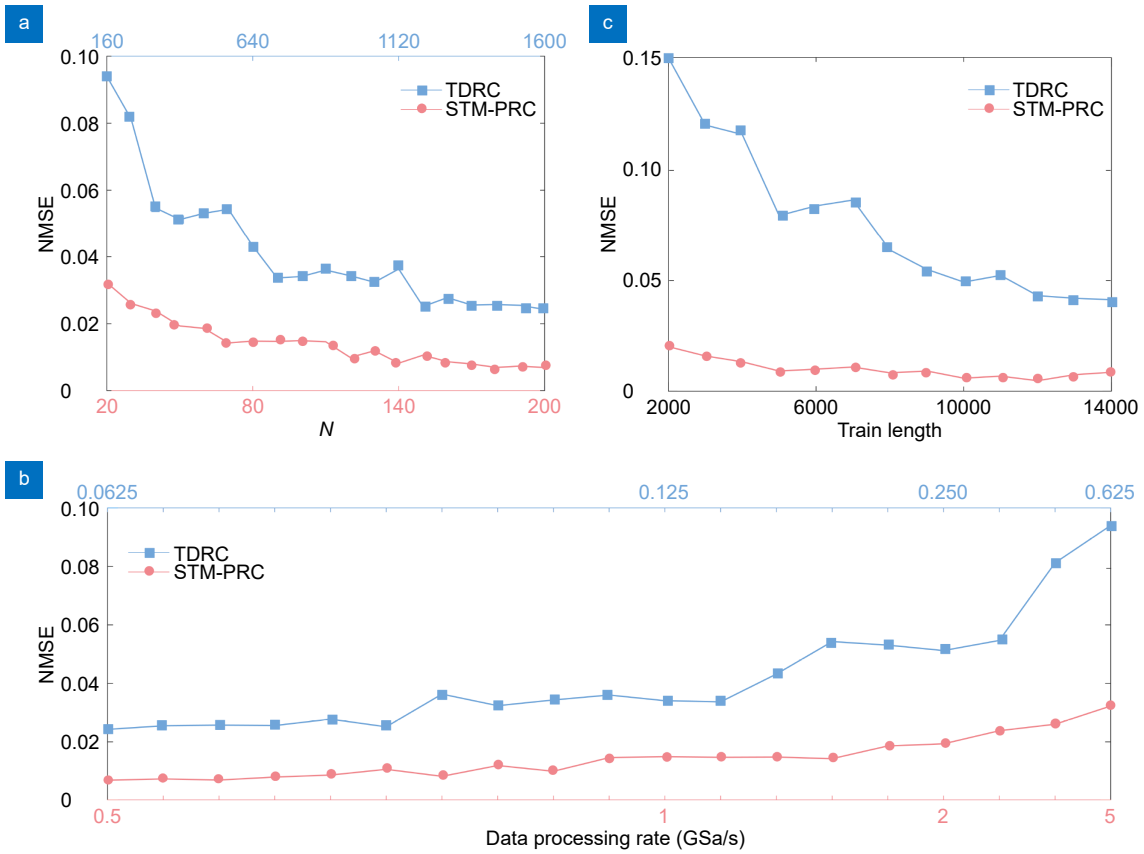

Fig. 5 | Prediction accuracy NMSE of STM-PRC and TDRC with different (**a**) number of virtual nodes; (**b**) data processing rate; (**c**) training length.

factor of $p_{\mathrm{f}} = 0.9$. The results clearly indicate that the STM-PRC architecture achieves accurate predictive performance over a broader parameter range, thereby reducing the need for meticulous parameter tuning and demonstrating enhanced practicality and robustness. In addition, the NMSE trends of STM-PRC and conventional TDRC remain largely consistent across comparable parameter intervals. On the one hand, excessively large feedback strength $k_{\mathrm{f,r}}$ can trigger strong chaotic dynamics, which in turn degrades the predictive performance of the reservoir. Conversely, an insufficient current factor p_{f} weakens the nonlinear response of the system, diminishing its sensitivity to subtle variations in the input signal and ultimately limiting prediction accuracy. Moreover, strong optical injection from the drive laser, together with an appropriate negative frequency detuning between the drive and reservoir lasers, can induce injection locking, thereby stabilizing the system dynamics and further improving prediction performance.

In addition to the processing speed, training dataset size and parameter optimization, the complexity of the high-dimensional dynamics being predicted also impacts prediction accuracy. Even with an identical topology, network dynamics with varying complexities show differences in predictive performance. To address this, we introduce normalized permutation entropy $PE(m) = -\sum_{r=1}^{m!} p(\pi_r)\log(p(\pi_r))/\log(m!)$ as a metric for evaluating the complexity of high-dimensional dynamics, where $PE(m) = 0$ corresponding to a regular, predictable dynamics, and $PE(m) = 1$ to a fully random and unpredictable one[49,50]. PE is particularly effective for analyzing time series that exhibit strong nonlinear characteristics and complex dynamic behaviors, and higher values of $PE(m)$ indicate greater randomness and increased complexity in the SL network. We chose PE over approximate entropy or fuzzy entropy because it is especially well-suited for nonlinear and complex signals and is more robust against small noise perturbations. By contrast, approximate entropy often lacks sufficient discriminability for nonlinear dynamics, while fuzzy entropy involves higher computational complexity and is highly sensitive to the choice of fuzzy parameters, making cross-scheme comparisons less consistent. In practice, PE is calculated by reconstructing the time series in phase space using the embedding dimension m and time

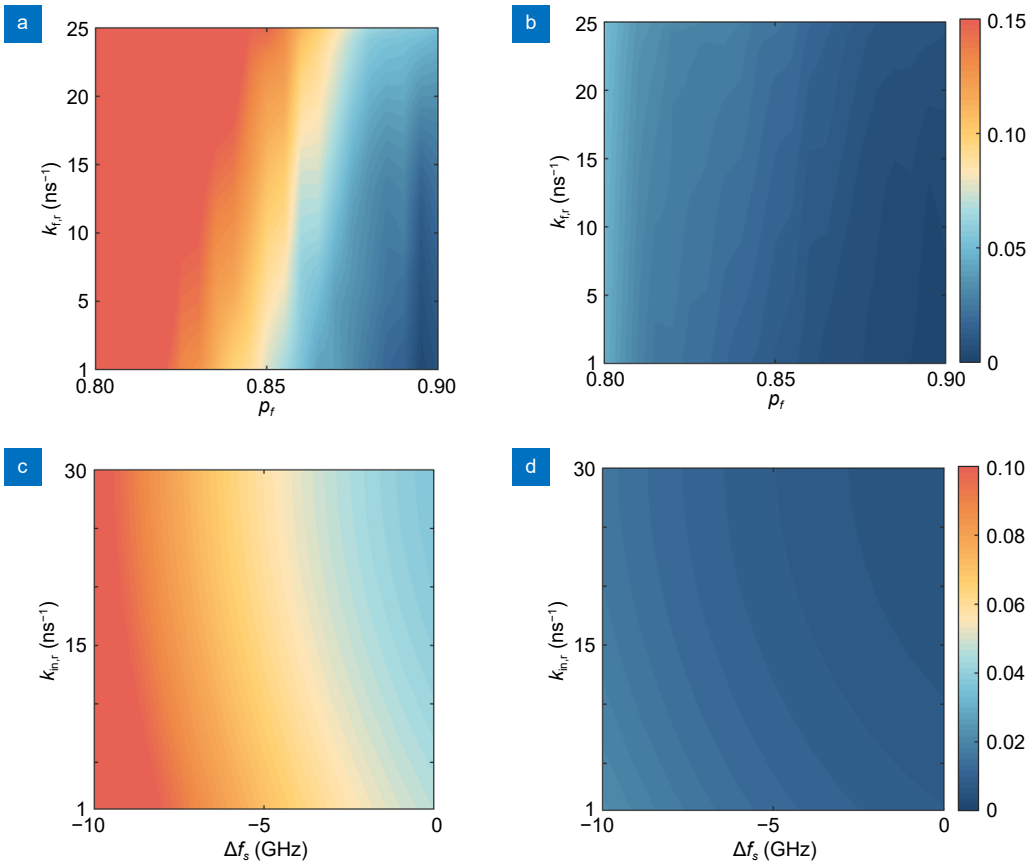

Fig. 6 | Two-dimensional evolution of NMSE in parameter spaces of p_f×$k_{f,r}$ and Δf_s×$k_{in,r}$ for conventional TDRC (**a**, **c**) and STM-PRC (**b**, **d**).

delay l. In this work, we set $m = 3, l = 1$ to evaluate the complexity of the SL network. Figure 7(a–d) explore how the complexity of network dynamics and prediction accuracy vary with the internal network operating parameters such as linewidth enhancement factor α_m, coupling strength σ_m, feedback strength $k_{m,f}$ and current factor $p_{f,m}$, respectively. The results clearly indicate that increased parameter values correspond to higher network complexity (PE) and elevated NMSE. More complex network dynamics place greater demands on the nonlinear mapping and memory capabilities of the RC system. As a result, the prediction accuracy declines as the complexity of the network dynamics increases.

Furthermore, we demonstrate that the STM-PRC prediction scheme is universally applicable to various network topologies, different node degrees and large-scale networks. Conventional TDRC is a purely data-driven approach that does not leverage the physical model information underlying the original data generation. However, in STM-PRC, we incorporate the coupling relationships between SLs, which allows for the effective capture of the dynamic behavior of the SL network. As shown in Fig. 8(a), while the conventional TDRC fails to accurately predict the dynamics characteristics of a complex network with 20 SLs, STM-PRC maintains high predictive performance. Meanwhile, to further validate its robustness, we demonstrate that STM-PRC maintains high predictive accuracy across various settings of network node degrees, as shown in Fig. 8(b). Additionally, the STM-PRC scheme decompose the prediction of high-dimensional dynamics into independent simplified RC parallelly, which enables efficient parallelization of the training process. This lightweight nature provides the system with excellent scalability, making it adaptable to large-scale networks. As shown in Fig. 8(c), the prediction performance of conventional TDRC deteriorates rapidly as the SL network size increases, while STM-PRC consistently maintains stable and high prediction accuracy, which confirms the generality and scalability of STM-PRC mechanism.

Dimensionality reduction method for high-dimensional spatial sequences

The topology of complex SL networks is intimately

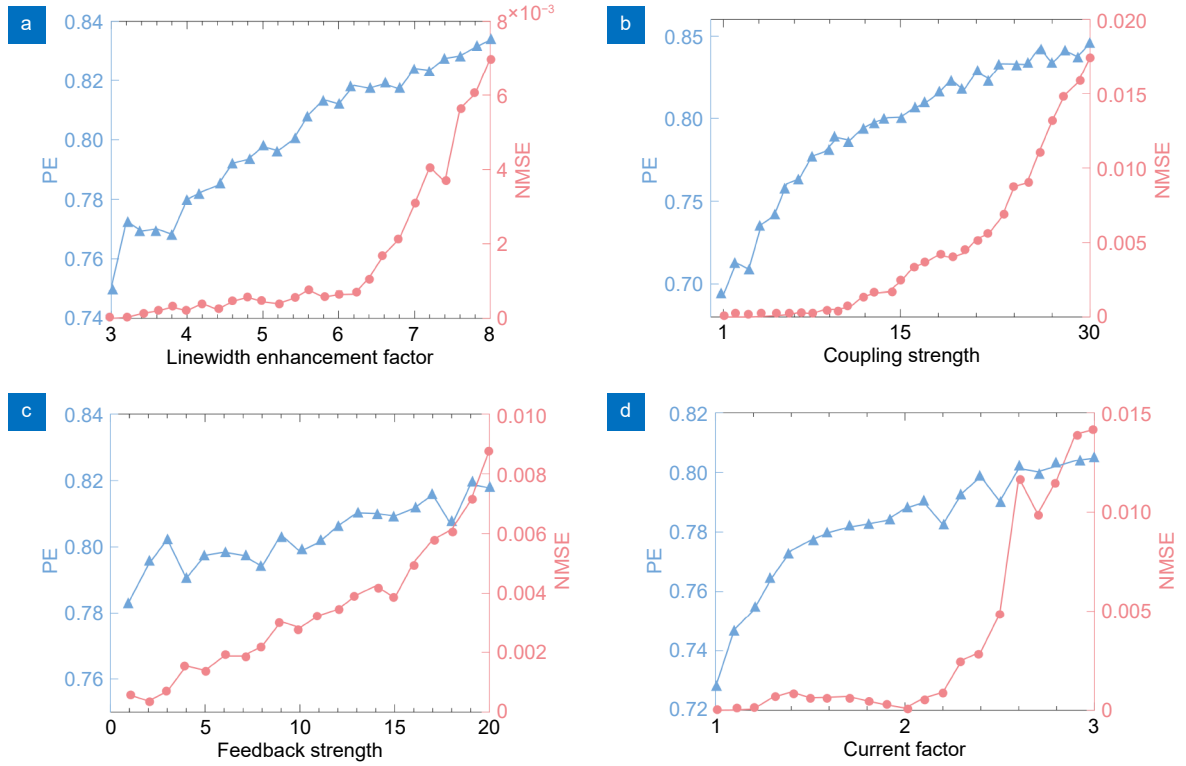

Fig. 7 | PE and NMSE versus linewidth enhancement factor σ_m (**a**). Coupling strength σ_m (**b**). Feedback strength $k_{f,m}$ (**c**). Current factor $p_{f,m}$ (**d**) for the topology illustrated in Fig. 1(a) under fixed simulation conditions α_m = 5, $p_{f,m}$ = 2.5, σ_m = 15 ns^{-1}, $k_{f,m}$ = 10 ns^{-1}.

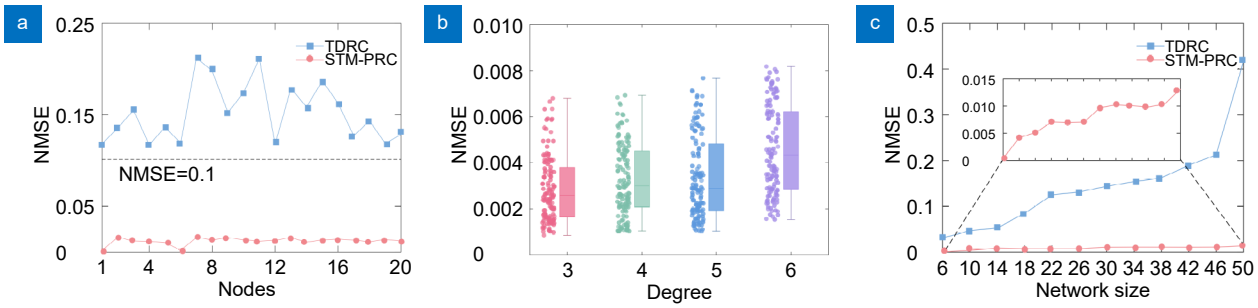

Fig. 8 | Scalability of STM-PRC with network size and node degree. (**a**) Prediction accuracy for each node using TDRC and STM-PRC methods in a 20-node SL network (node degree = 3, (N = 2000, $N_{p,i}$ = 100each)). (**b**) Prediction performance of STM-PRC across 20-node SL networks with varying node degrees. (**c**) Comparison of prediction performance between TDRC and STM-PRC across SL networks of different sizes.

associated with their synchronization behavior, and effectively exploiting this property can further reduce the dimensionality of high-dimensional chaotic data[44,51,52]. From a group-theoretic perspective, network symmetries can be rigorously characterized using permutation matrices $\boldsymbol{R}_g$. Mathematically, a permutation matrix $\boldsymbol{R}_g$ applied to the network's adjacency matrix $\boldsymbol{A}$ rearranges the SL nodes without altering the adjacent characteristics, thus satisfying $\boldsymbol{R}_g\boldsymbol{A} = \boldsymbol{A}\boldsymbol{R}_g$[53]. Identifying these symmetries and their corresponding orbits enables the division of the SL network into distinct synchronized clusters. SLs within each cluster will remain synchronized under identical initial conditions for the equivalent dynamical equations, while stable cluster synchronization depends on network parameters with random initial conditions for symmetry breaking. Figure 9(a) illustrates a network consists of 14 SLs, grouped into five non-trivial clusters represented by distinct colors $C_1 = \{1, 2, 4, 12\}$, $C_2 = \{3, 5\}$, $C_3 = \{6, 7, 8, 13\}$, $C_4 = \{9, 10\}$, $C_5 = \{11, 14\}$. If the adjacency matrix $\boldsymbol{A} \in \mathbb{R}^{N\times N}$ and $\boldsymbol{A}_s \in \mathbb{R}^{M\times M}$(where N is the number of network nodes and M is the number of synchronized clusters), then $\boldsymbol{A}_{\text{smn}} = \sum_{j\in C_n} \boldsymbol{A}_{ij}, i \in C_m$. Here, the adjacency matrix $\boldsymbol{A}$ is

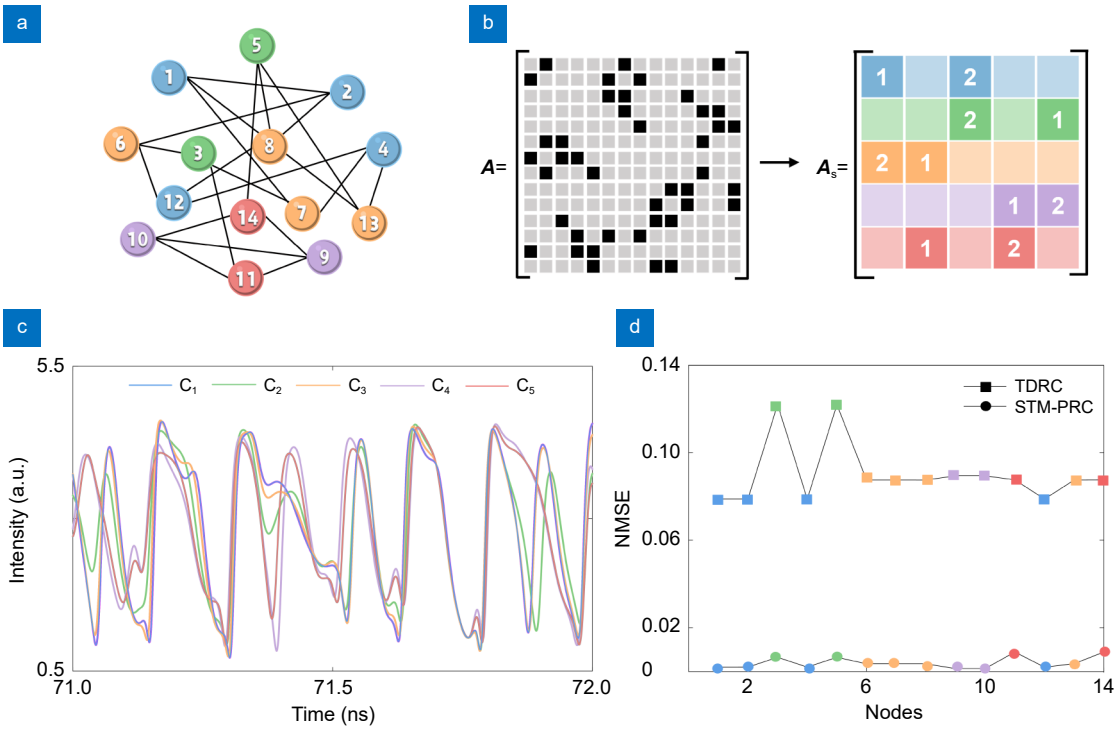

Fig. 9 | (**a**, **b**) Schematic diagram of the complex SL network topology, where nodes of identical color belong to the same synchronization cluster. (**c**) Output dynamics of SL nodes corresponding to the network in (a), with α_m = 3, $k_{f,m}$ = 9 ns^{-1}, σ_m = 8.2 ns^{-1}, $p_{f,m}$ = 2.5. (**d**) Prediction of synchronization phenomena in SL network.

reduced to $\boldsymbol{A}_s$, as shown in Fig. 9(b). Figure 9(c) shows that, despite the presence of 14 individual SLs, the network outputs converge to five isolated dynamical trajectories, indicating stable isochronous synchronization within each cluster. We show that leveraging these inherent symmetries could simplify the complex coupling relationships, effectively reducing the dimensionality of the chaotic time-series prediction task and thereby enhancing computational efficiency. Figure 9(d) illustrates the practical utility of this concept by employing only five parallel TDRC systems to accurately forecast the dynamics of the SL network shown in Fig. 9(a), thereby demonstrating that synchronization-based dimensionality reduction enables precise prediction of SL network dynamics with fewer parallel reservoirs. This approach preserves high prediction accuracy while enhancing computational efficiency and optimizing resource utilization in the STM-PRC configuration, thereby making hardware implementation more feasible and practical.

Experimental demonstration

Figure 10 illustrates the all-fiber STM-PRC experimental setup based on SLs for predicting the chaotic dynamics of each node in SL networks. A distributed feedback laser (DFB, KG-BF-1550-F-S-FA) is utilized as the drive laser (DL). The output of DL passes through an optical isolator (OI) to suppress back reflections, preserving laser stability and output beam quality. A polarization controller is then implemented to align the polarization state of the optical signal, thereby reducing polarization-related losses and improving system efficiency. An arbitrary waveform generator (AWG, M8195A, 65GSa/s) synthesizes the masked input signal, which is subsequently intensity-modulated onto the optical carrier using a Mach-Zehnder modulator (MZM). The MZM is accurately biased at its quadrature point through precise voltage adjustments to ensure optimal modulation stability and performance. The modulated optical signal is amplified by an erbium-doped fiber amplifier (EDFA) and then split by a 20:80 optical coupler (OC). One branch is directed towards a power meter (PM) for real-time monitoring, and the other branch injects the signal into a reservoir laser through a circulator. On the other hand, the output of the reservoir laser is subsequently split by a 50:50 OC, with one portion fed back into the reservoir loop through a 20:80 OC as a self-feedback and the other directed to a photodetector (PD). The detected signal is recorded using a high-speed digital signal analyzer

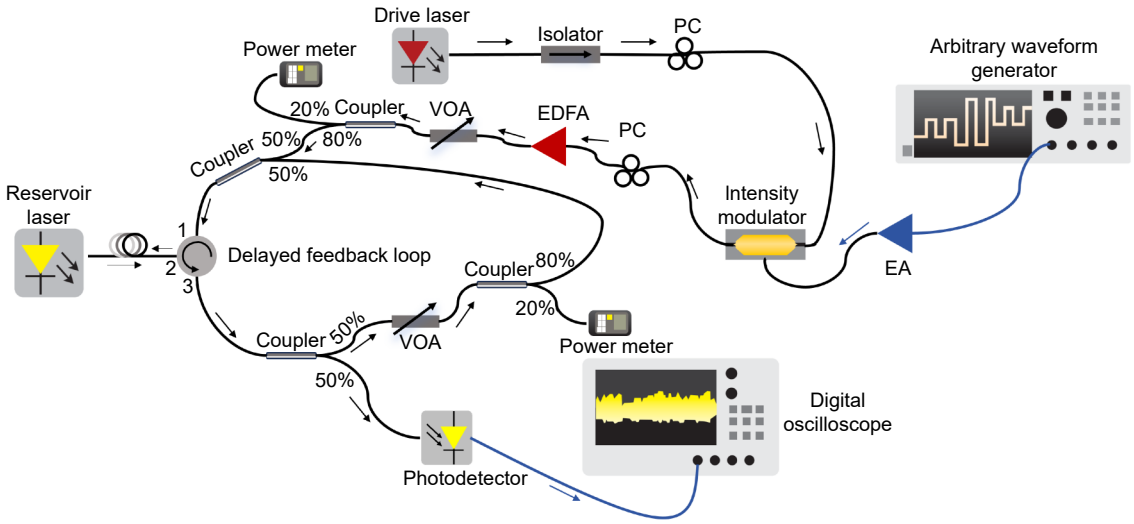

Fig. 10 | Schematic of the experimental STM-PRC setup for each node.

(Agilent, DSA91304, 40 GSa/s). Both injected and self-feedback optical signal intensities are meticulously controlled using variable optical attenuators (VOA) and verified with a power meter to maintain experimental precision.

During the experimental process, the optical delay of the reservoir laser was fixed at 77.3 ns, with the temperatures of the drive laser and the reservoir laser maintained at 23 °C and 21.9 °C, and the bias currents were set to be 25 mA and 5 mA, respectively. The optical spectrum was measured by an optical spectrum analyzer (Yokogawa), with the central wavelengths of the drive laser and reservoir laser being 1548.752 nm and 1548.658 nm, respectively. Regarding the implementation of the reservoir, the conventional TDRC employing a "multi-input, multi-output" configuration with $u(t) \in \mathbb{R}^8$ and $y(t+\Delta t) \in \mathbb{R}^8$ for the prediction of high-dimensional chaotic dynamics of complex SL networks in Fig. 1(a). In contrast, the STM-PRC decomposes the prediction into 8 independent simplified RC parallelly with $u_{p,i}(t) \in \mathbb{R}^{D_i+1}$ and $y_{p,i}(t+\Delta t) \in \mathbb{R}^1$. Considering experimental simplicity, instead of constructing eight separate reservoirs, the STM-PRC experiment was implemented using a single simplified RC, with eight different input signals corresponding to the input information of the eight nodes.

To demonstrate the effectiveness of the STM-PRC scheme for forecasting of the high-dimensional spatiotemporal dynamics generated by SL network. Figure 11 experimentally compares the prediction performance between conventional TDRC and STM-PRC configurations across variations in key experimental parameters, including injection strength $k_{in,r}$, feedback strength $k_{f,r}$, detuning frequency Δf_s, and bias current J. The blue line denotes NMSE values obtained from the conventional TDRC, while red line plots represent NMSE results from our parallel configuration consisting of eight SLs. Experimental results illustrate the parallel STM-PRC configuration consistently maintains high predictive accuracy across diverse experimental conditions. This robust performance underscores the enhanced flexibility and capability of STM-PRC in accommodating parameter variations. Consequently, these findings confirm the superior predictive efficiency and accuracy of STM-PRC over conventional isolated TDRC, highlighting its potential for effectively modeling and forecasting complex SL network dynamics.

To further validate the generality of STM-PRC, we evaluate its performance on high-dimensional chaotic time series generated from a physical experimental system. As depicted in Fig. 12, the experimental setup for generating high-dimensional chaotic dynamics comprises a SL network consisting of three SLs. Specifically, SL_1 (DFB, KG-BF-1550-F-S-FA) operates at a central wavelength of 1549.382 nm with a bias current of 10 mA. In contrast, SL_2 and SL_3 (KG-BF-1550-F-S-FA) is tuned to a slightly shifted central wavelength of 1549.386 nm, while retaining the same bias current of 10 mA. SL_1 is mutually coupled to SL_2 and SL_3 as shown in Fig. 13(a) and the coupling strength between these lasers is precisely controlled using variable optical attenuators. Each of the three SL outputs is independently detected by a photodetector (PD) and subsequently sampled using a high-speed digital signal analyzer (Agilent, DSA91304,

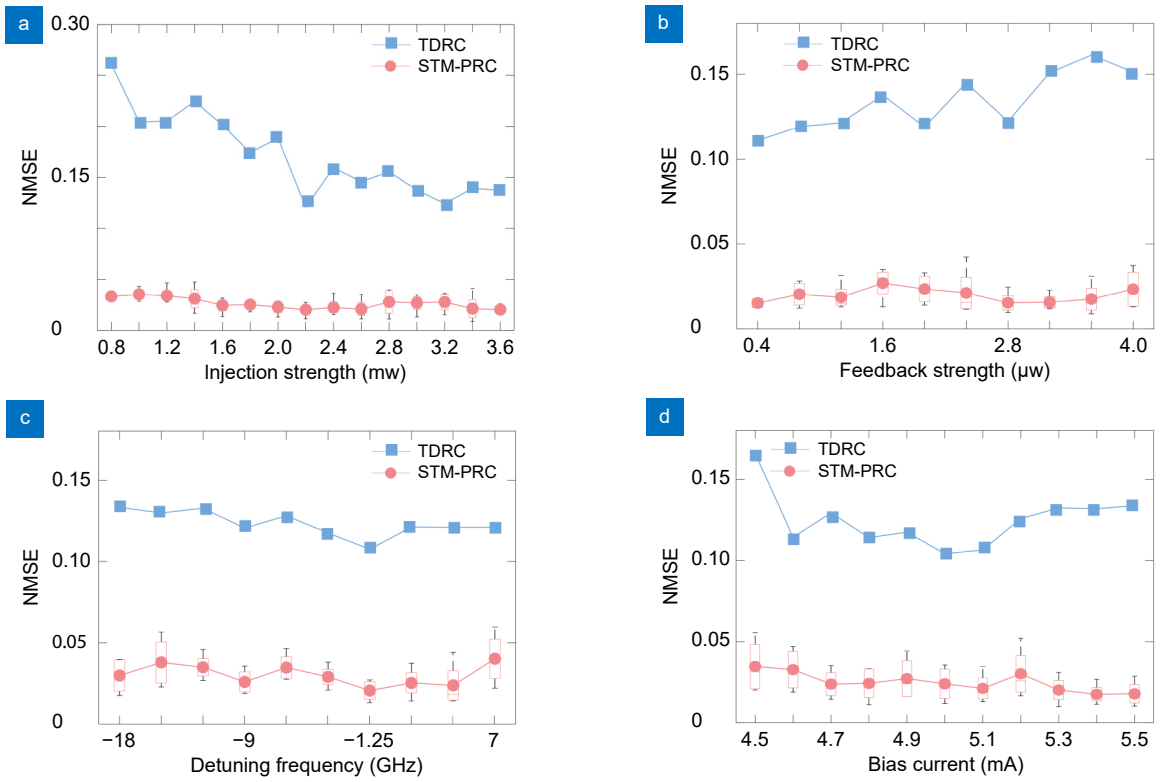

Fig. 11 | Predictive performance NMSE of traditional TDRC and STM-PRC under variations in (**a**) injection strength $k_{in,r}$ with $k_{f,r}$ = 1.6 μw, (**b**) feedback strength $k_{f,r}$ with $k_{in,r}$ = 3 mw, (**c**) detuning frequency Δf_s, and (**d**) bias current J both with $k_{in,r}$ = 2 mw, $k_{f,r}$ = 1.6 μw. For all cases considered, N = 240, $N_{p,i}$ = 30.

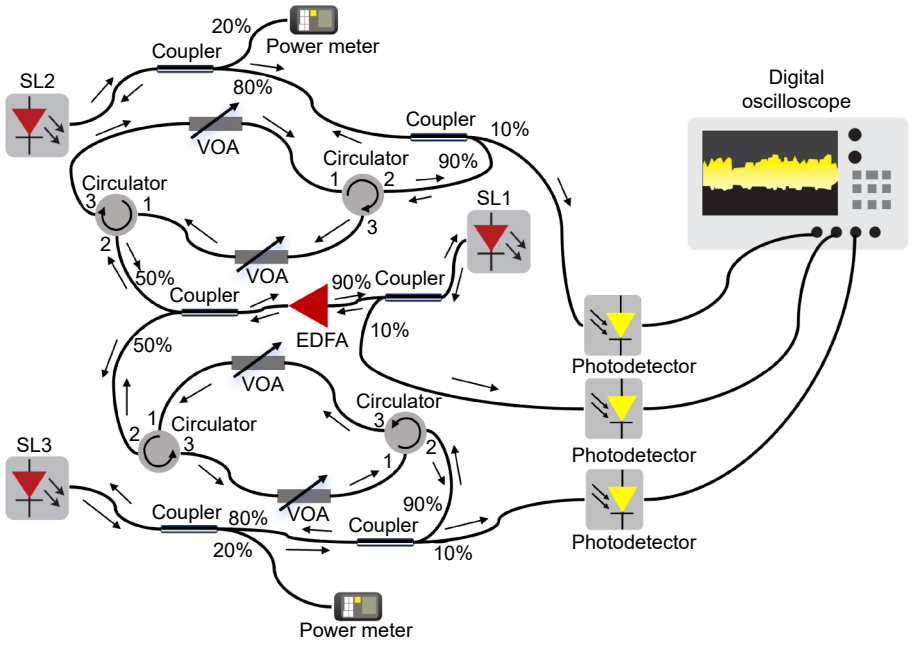

Fig. 12 | The experimental setup for synchronization of an undirected SL network consisting of three SLs.

40 GSa/s).

Furthermore, to validate the feasibility of the proposed dimensionality reduction method, the cross-correlation function (CCF) is introduced to quantitatively assess the stability of cluster synchronization in SL network. This function is defined by calculating the correlation coefficient between the dynamics of the SLs within the same cluster, as expressed in Eq. (11):

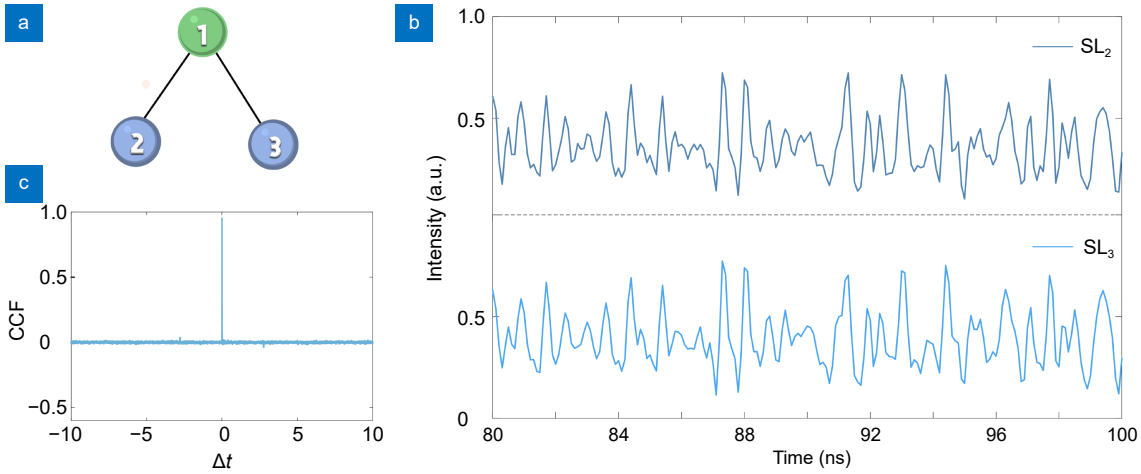

Fig. 13 | (**a**) Topology for network composed of three SLs. (**b**) Dynamical evolution of SL_2 and SL_3 in SL network. (**c**) Cross-correlation function (CCF) of SL_2 and SL_3.

$$C_{m,n} = \frac{\langle (I_m(t+\Delta t) - \langle I_m(t+\Delta t)\rangle)\cdot(I_n(t) - \langle I_n(t)\rangle)\rangle}{\sqrt{\langle (I_m(t+\Delta t) - \langle I_m(t+\Delta t)\rangle)^2\rangle \cdot \langle (I_n(t) - \langle I_n(t)\rangle)^2\rangle}}, \tag{11}$$

where $I_m = |E_2(t)^2|$ and $I_n = |E_3(t)^2|$ represent the optical intensity of SL_2 and SL_3 respectively, $\langle\cdot\rangle$ stands for time averaging, Δt is the varying shift time. The maximum value of the CCF represents the degree of correlation in the range of $\Delta t = [-20\ \text{ns}, -20\ \text{ns}]$. Figure 13(b) presents the dynamical evolution of SL_2 and SL_3 under the aforementioned operating conditions. As observed in Fig. 13(c), isochronous between SL_2 and SL_3 within the same cluster is achieved, as evidenced by the overlapping of chaotic trajectories. Consequently, the complexity of forecasting tasks within this SL network can be effectively simplified, reducing from the prediction of three separate chaotic time series to forecasting the dynamics of two synchronized clusters.

Figure 14 presents the predictive performance of the STM-PRC architecture for two synchronized clusters: $C_1 = \{1\}$ and $C_2 = \{2, 3\}$. In C_2, since SL_2 and SL_3 are already synchronized, we only need to predict the output of either SL_2 or SL_3. Specifically, Fig. 14(a) shows the prediction results for SL_1 in cluster C_1, while Fig. 14(b) presents the prediction results for SL_2 in cluster C_2, which can also represent SL_3. The achieved prediction accuracies, measured by NMSE, are 0.032 and 0.0219, respectively. These results confirm the feasibility of synchronized dimensionality reduction, enabling significant simplification of the parallel STM-PRC structure while preserving high prediction accuracy. This approach further enhances the system's computational efficiency.

Conclusions

In this work, we propose and experimentally validate a STM-PRC architecture based on spatiotemporal multiplexing for accurate forecasting of high-dimensional chaotic dynamics in complex SL networks. By leveraging the intrinsic network topological characteristics, we

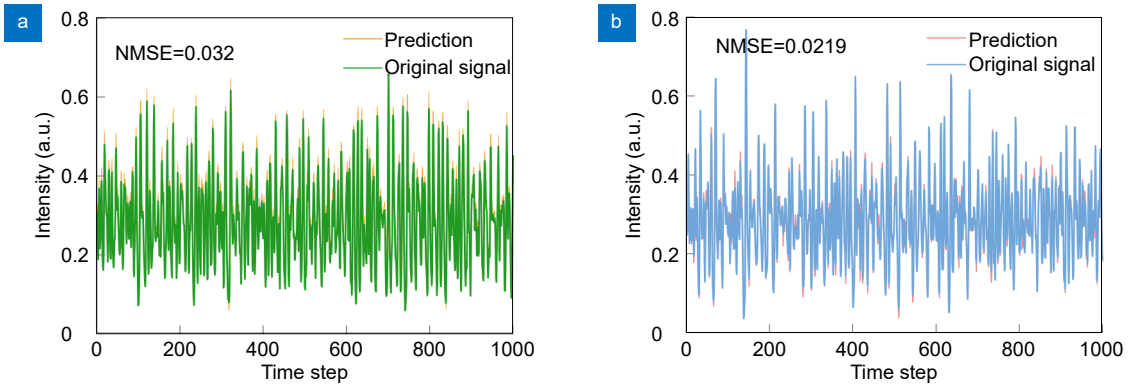

Fig. 14 | The prediction performance of the two synchronized clusters. (**a**) Cluster C_1 = {1}. (**b**) Cluster C_2 = {2, 3}.

strategically decompose the high-dimensional prediction task into parallel, simplified, and independent reservoir computing modules. This approach effectively addresses the challenges associated with predicting high-dimensional chaotic dynamics, enabling both accelerated processing and hardware-friendly implementation. Moreover, a dimensionality reduction method based on network symmetry and synchronization theory is introduced to significantly reduce the complexity of chaotic time-series prediction, thereby enhancing the computational efficiency of STM-PRC and enabling its scalable deployment in large-scale photonic systems. Finally, the generality of the STM-PRC architecture is validated through the prediction of high-dimensional chaotic dynamics experimentally generated in SL networks. Chaotic optical communication offers significant potential for physical-layer secure transmission but is currently constrained by hardware mismatches and synchronization challenges in high-speed, long-distance links. To overcome these limitations, AI-based chaotic optical communication schemes[54,55] have been developed, which are compatible with high-speed coherent optical fiber systems and can enhance transmission security with low complexity and cost. Looking forward, as next-generation optical networks evolve toward increased complexity and heterogeneity, the ability to predict the spatiotemporal dynamics of SL networks could provide valuable opportunities for advancing chaos-based all-optical secure communication.

References

1. Chen RX, Shu HW, Shen BT et al. Breaking the temporal and frequency congestion of LiDAR by parallel chaos. *Nat Photonics* **17**, 306–314 (2023).
2. Tang X, Xia GQ, Ran C et al. Fast physical random bit generation based on a broadband chaotic entropy source originated from a filtered feedback WRC-FPLD. *IEEE Photonics J* **11**, 7800710 (2019).
3. Argyris A, Syvridis D, Larger L et al. Chaos-based communications at high bit rates using commercial fibre-optic links. *Nature* **438**, 343–346 (2005).
4. Jiang N, Wang YJ, Zhao AK et al. Simultaneous bandwidth-enhanced and time delay signature-suppressed chaos generation in semiconductor laser subject to feedback from parallel coupling ring resonators. *Opt Express* **28**, 1999–2009 (2020).
5. Xiang SY, Shi YC, Guo XX et al. Hardware-algorithm collaborative computing with photonic spiking neuron chip based on an integrated Fabry-Perot laser with a saturable absorber. *Optica* **10**, 162–171 (2023).
6. Wang LS, Wang JL, Wu YS et al. Chaos synchronization of semiconductor lasers over 1040-km fiber relay transmission with hybrid amplification. *Photonics Res* **11**, 953–960 (2023).
7. Liu HX, Pan BC, Huang YS et al. Ultra-compact lithium niobate photonic chip for high-capacity and energy-efficient wavelength-division-multiplexing transmitters. *Light Adv Manuf* **4**, 13 (2023).
8. Guo Y, Cai Q, Li P et al. Ultrafast and real-time physical random bit extraction with all-optical quantization. *Adv Photonics* **4**, 035001 (2022).
9. Wei C, Yu YR, Wang ZY et al. Ultra-wideband waveguide-coupled photodiodes heterogeneously integrated on a thin-film lithium niobate platform. *Light Adv Manuf* **4**, 30 (2023).
10. Xiang SY, Shi YC, Zhang YH et al. Photonic integrated neuro-synaptic core for convolutional spiking neural network. *Opto-Electron Adv* **6**, 230140 (2023).
11. Deng Y, Fan ZF, Zhao BB et al. Mid-infrared hyperchaos of interband cascade lasers. *Light Sci Appl* **11**, 7 (2022).
12. Kanno K, Uchida A, Bunsen M. Complexity and bandwidth enhancement in unidirectionally coupled semiconductor lasers with time-delayed optical feedback. *Phys Rev E* **93**, 032206 (2016).
13. Zhao AK, Jiang N, Peng JF et al. Parallel generation of low-correlation wideband complex chaotic signals using CW laser and external-cavity laser with self-phase-modulated injection. *Opto-Electron Adv* **5**, 200026 (2022).
14. Li XZ, Zhuang JP, Li SS et al. Randomness evaluation for an optically injected chaotic semiconductor laser by attractor reconstruction. *Phys Rev E* **94**, 042214 (2016).
15. Li NQ, Zunino L, Locquet A et al. Multiscale ordinal symbolic analysis of the Lang-Kobayashi model for external-cavity semiconductor lasers: a test of theory. *IEEE J Quantum Electron* **51**, 2200206 (2015).
16. Miranian A, Abdollahzade M. Developing a local least-squares support vector machines-based neuro-fuzzy model for nonlinear and chaotic time series prediction. *IEEE Trans Neural Netw Learn Syst* **24**, 207–218 (2013).
17. Chakraborty K, Mehrotra K, Mohan CK et al. Forecasting the behavior of multivariate time series using neural networks. *Neural Netw* **5**, 961–970 (1992).
18. Karunasinghe DSK, Liong SY. Chaotic time series prediction with a global model: artificial neural network. *J Hydrol* **323**, 92–105 (2006).
19. De Oliveira KA, Vannucci Á, da Silva EC. Using artificial neural networks to forecast chaotic time series. *Phys A Stat Mech Appl* **284**, 393–404 (2000).
20. Sun Y, Zhang LY, Yao MH. Chaotic time series prediction of nonlinear systems based on various neural network models. *Chaos Solitons Fractals* **175**, 113971 (2023).
21. Ramadevi B, Bingi K. Chaotic time series forecasting approaches using machine learning techniques: a review. *Symmetry* **14**, 955 (2022).
22. Pathak J, Hunt B, Girvan M et al. Model-free prediction of large spatiotemporally chaotic systems from data: a reservoir computing approach. *Phys Rev Lett* **120**, 024102 (2018).
23. Srinivasan K, Coble N, Hamlin J et al. Parallel machine learning for forecasting the dynamics of complex networks. *Phys Rev Lett* **128**, 164101 (2022).
24. Weng TF, Yang HJ, Gu CG et al. Synchronization of chaotic systems and their machine-learning models. *Phys Rev E* **99**, 042203 (2019).
25. Li XZ, Yang B, Zhao S et al. On prediction of chaotic dynamics in semiconductor lasers by reservoir computing. *Opt Express* **31**, 40592–40603 (2023).
26. Cunillera A, Soriano MC, Fischer I. Cross-predicting the dynamics of an optically injected single-mode semiconductor laser using reservoir computing. *Chaos* **29**, 113113 (2019).
27. Appeltant L, Soriano MC, Van der Sande G et al. Information

processing using a single dynamical node as complex system. *Nat Commun* **2**, 468 (2011).
28. Cai Q, Guo Y, Li P et al. Modulation format identification in fiber communications using single dynamical node-based photonic reservoir computing. *Photonics Res* **9**, B1–B8 (2021).
29. Shen YW, Li RQ, Liu GT et al. Deep photonic reservoir computing recurrent network. *Optica* **10**, 1745–1751 (2023).
30. Bueno J, Maktoobi S, Froehly L et al. Reinforcement learning in a large-scale photonic recurrent neural network. *Optica* **5**, 756–760 (2018).
31. Zhou CD, Huang Y, Yang YG et al. Streamlined photonic reservoir computer with augmented memory capabilities. *Opto-Electron Adv* **8**, 240135 (2025).
32. Tan XS, Hou YS, Wu ZM et al. Parallel information processing by a reservoir computing system based on a VCSEL subject to double optical feedback and optical injection. *Opt Express* **27**, 26070–26079 (2019).
33. Cai DY, Huang Y, Yang YG et al. Enhanced performances of photonic reservoir computing using a semiconductor laser with random distributed optical feedback. *Opt Lett* **48**, 6392–6395 (2023).
34. Yang YG, Zhou P, Mu PH et al. Time-delayed reservoir computing based on an optically pumped spin VCSEL for high-speed processing. *Nonlinear Dyn* **107**, 2619–2632 (2022).
35. Li XY, Jiang N, Zhang Q et al. Performance-enhanced time-delayed photonic reservoir computing system using a reflective semiconductor optical amplifier. *Opt Express* **31**, 28764–28777 (2023).
36. Guo XX, Xiang SY, Cao XY et al. Experimental and numerical demonstration of hierarchical time-delay reservoir computing based on cascaded VCSELs with feedback and multiple injections. *Sci China Inf Sci* **67**, 122403 (2024).
37. Hasegawa H, Kanno K, Uchida A. Parallel and deep reservoir computing using semiconductor lasers with optical feedback. *Nanophotonics* **12**, 869–881 (2023).
38. Li SS, Li JW, Zou XH et al. Photonic reservoir computing using a self-injection locked semiconductor laser under narrowband optical feedback. *Opt Lett* **48**, 2006–2009 (2023).
39. Amil P, Soriano MC, Masoller C. Machine learning algorithms for predicting the amplitude of chaotic laser pulses. *Chaos* **29**, 113111 (2019).
40. Li XZ, Sheng B, Zhang M. Predicting the dynamical behaviors for chaotic semiconductor lasers by reservoir computing. *Opt Lett* **47**, 2822–2825 (2022).
41. Kai C, Li P, Yang Y et al. Forecasting the chaotic dynamics of external cavity semiconductor lasers. *Opt Lett* **48**, 1236–1239 (2023).
42. Guo XX, Zhou HX, Xiang SY et al. Short-term prediction for chaotic time series based on photonic reservoir computing using VCSEL with a feedback loop. *Photonics Res* **12**, 1222–1230 (2024).
43. Zhang LY, Huang CK, Li SS et al. Heterogeneous forecasting of chaotic dynamics in vertical-cavity surface-emitting lasers with knowledge-based photonic reservoir computing. *Photonics Res* **13**, 728–736 (2025).
44. Zhang LY, Pan W, Yan LS et al. Cluster synchronization of coupled semiconductor lasers network with complex topology. *IEEE J Sel Top Quantum Electron* **25**, 1501007 (2019).
45. Lang R, Kobayashi K. External optical feedback effects on semiconductor injection laser properties. *IEEE J Quantum Electron* **16**, 347–355 (1980).
46. Kuriki Y, Nakayama J, Takano K et al. Impact of input mask signals on delay-based photonic reservoir computing with semiconductor lasers. *Opt Express* **26**, 5777–5788 (2018).
47. Tang JY, Lin BD, Shen YW et al. Asynchronous photonic time-delay reservoir computing. *Opt Express* **31**, 2456–2466 (2023).
48. Zhang LY, Peng L, Li SS et al. Hybrid parallel photonic reservoir computing with accelerated data processing speed. *Opt Laser Technol* **175**, 110830 (2024).
49. Bandt C, Pompe B. Permutation entropy: a natural complexity measure for time series. *Phys Rev Lett* **88**, 174102 (2002).
50. Xiang SY, Pan W, Yan LS et al. Quantifying chaotic unpredictability of vertical-cavity surface-emitting lasers with polarized optical feedback via permutation entropy. *IEEE J Sel Top Quantum Electron* **17**, 1212–1219 (2011).
51. Zhang LY, Motter AE, Nishikawa T. Incoherence-mediated remote synchronization. *Phys Rev Lett* **118**, 174102 (2017).
52. Liu SQ, Jiang N, Zhao AK et al. Secure optical communication based on cluster chaos synchronization in semiconductor lasers network. *IEEE Access* **8**, 11872–11879 (2020).
53. Pecora LM, Sorrentino F, Hagerstrom AM et al. Cluster synchronization and isolated desynchronization in complex networks with symmetries. *Nat Commun* **5**, 4079 (2014).
54. Jiang L, Feng JC, Yan LS et al. Chaotic optical communications at 56 Gbit/s over 100-km fiber transmission based on a chaos generation model driven by long short-term memory networks. *Opt Lett* **47**, 2382–2385 (2022).
55. Feng JC, Jiang L, Sun JH et al. 256 Gbit/s chaotic optical communication over 1600 km using an AI-based optoelectronic oscillator model. *J Lightwave Technol* **42**, 2774–2783 (2024).

Acknowledgements

This work was supported in part by National Natural Science Foundation of China under Grant (Nos. 62431024, U22A2089, 62375228), Sichuan Science Fund for Distinguished Young Scholars (2023NSFSC1969), Fundamental Research Funds for the Central Universities (2682025ZTPY058).

Author contributions

T. Yang and L. Y. Zhang contributed to the idea, conducted the experiments and the writing of the manuscript. L. S. Yan, L. Y. Zhang, and S. S. Li supervised and directed the research. L. S. Yan, W. Pan, and X. H. Zou were responsible for funding acquisition. All authors discussed the results and commented on the manuscript.

Competing interests

The authors declare no competing financial interests.

Supplementary information

Supplementary information for this paper is available at https://doi.org/10.29026/oea.2025.250159

Scan for Article PDF